

Devitrification and Melting Dynamics in Vapor Deposited Water Ice

Fabio Leoni,^{1,*} Fausto Martelli,^{2,3,1} and John Russo¹

¹*Dipartimento di Fisica, Università degli Studi di Roma La Sapienza, Piazzale Aldo Moro 5, Rome, 00185, Italy*

²*IBM Research Europe, Hartree Centre, Daresbury WA4 4AD, UK*

³*CNR-Istituto dei Sistemi Complessi, Piazzale Aldo Moro 5, Rome, 00185, Italy*

The equilibration dynamics of ultrastable glasses subjected to heating protocols has attracted recent experimental and theoretical interest. With simulations of the mW water model, we investigate the devitrification and melting dynamics of both conventional quenched (QG) and vapor deposited (DG) amorphous ices under controlled heating ramps. By developing an algorithm to reconstruct hydrogen-bond networks, we show that bond ring statistics correlates with the structural stability of the glasses and allows tracking crystalline and liquid clusters during devitrification and melting. We find that QG melts in the bulk, whereas melting in DG preferentially begins near the free surface. During devitrification, the DG shows an excess of 5-membered rings near the free surface, which is consistent with its tendency to nucleate the crystal phase in this region. Additionally, the DG shows an Avrami exponent exceeding the standard $1+d$ behavior, while both glasses display the same sub-3d growth of liquid clusters across heating rates, indicating that the DG enhanced exponent stems from its higher kinetic stability.

I. INTRODUCTION

Since the experimental realization of ultrastable glasses (UGs) by vapor depositing molecules on a cold substrate [1], both experimental and computational studies have extensively explored the formation of UGs across various materials and model systems by tuning parameters such as the deposition rate and substrate temperature [2, 3], and more recently the substrate softness [4].

One of the most striking features distinguishing UGs from conventional quenched glasses (QG)—which are produced by rapidly cooling the liquid melt to avoid crystallization—is their enhanced kinetic stability [2, 3, 5–10]. This enhanced stability often manifests as a higher onset temperature T_o upon heating, with T_o the temperature at which the glass begins the transformation into the supercooled liquid, and has significant implications for technological applications where avoiding the deterioration of the glass properties over time is critical. In this work, we consider melting as the transition from a solid phase (either glassy or crystalline) to the liquid phase, while devitrification refers to the transformation from the glassy state into a crystalline phase, which can be mediated in some conditions by the formation of a supercooled liquid phase.

Only in recent years have experimental [11, 12] and computational [13–15] studies begun to address the equilibration dynamics of UGs subjected to heating ramps. A pivotal experimental advancement by Ruiz-Ruiz et al. [12] enabled real-time, microscopic-scale observation of melting in highly equilibrated glasses. Their results showed that melting in UGs proceeds heterogeneously in space, with sparse liquid-like regions separated by microscale distances (as also shown in Ref. [16] for indomethacin)—unlike QG, where such regions are spaced

at the nanoscale and their transformation into supercooled liquid upon heating is found to proceed more homogeneously [17]. From a computational standpoint, studies using Lennard-Jones (LJ) polydisperse systems have revealed that the equilibration dynamics of melting UGs differ markedly from both equilibrium relaxation and aging dynamics [14]. Deviations from classical Avrami kinetics [18] of the melting clusters have been observed in Ref. [14]. The increased stability of the glass, promoted by surface and subsurface mobility enhancement in vapor deposited materials [1, 19–25], has been shown to influence the crossover from bulk- to surface-mediated melting dynamics in both deposited and bulk UGs [13]. Molecular dynamics (MD) simulations of a polydisperse LJ glass [15] have shown that, even if the equilibration of the glass during heating proceeds by domain growth, there is no evidence to support a nucleation mechanism. Instead, melting has been found to proceed through local rearrangements which propagate mobility to neighborhoods [15], a process known as dynamic facilitation [17, 26–28]. The self-propagation of mobility can give rise to avalanches of plastic events [29] or displacements correlated in space and time [30]. An Avrami-like domain growth during heating ramps can still be derived from a dynamical facilitation description [15].

In a recent study [31], the authors have simulated via MD the formation of DG of tetrahedral materials—systems characterized by networks of strong directional bonds—using the generalized Stillinger-Weber (SW) potential [32]. This potential has been used to describe fundamental properties of several materials employed in the semiconductor and electronics industry such as germanium and silicon [33], and pure water [34, 35], especially in relation to ice nucleation and crystallization [36–38]. Results obtained in Ref. [31] demonstrated that DG in these systems can exhibit ultrastability, outperforming QG formed under equivalent thermodynamic conditions, within a temperature range constrained by crystal nucleation at higher temperatures.

* fabio.leoni@uniroma1.it

In this study, we focus on the devitrification and melting dynamics of both deposited and quenched glasses during heating ramps applied at different rates. We use the SW potential with parameters tailored to describe water, reducing it to the coarse-grained monatomic water (mW) model [39]. The study of amorphous water ices is of great interest in fields going from astrophysical and planetary science [40], to cryopreservation of biological systems [41], to the understanding of water anomalies and phase diagram [42].

Given that many thermodynamic, dynamic, and structural properties of water are influenced by its hydrogen-bond network (HBN) [43, 44], we develop a novel algorithm to assign oxygen-hydrogen (OH) bonds between mW point molecules. This framework enables us to analyze the resulting HBN, including ring statistics of varying orders. Several properties of water at different conditions, from the liquid to the solid phases, have been linked to features of its topological bond network [45, 46].

Moreover, by characterizing this HBN, we can identify energetically neighboring particles and trace the formation and evolution of crystalline clusters during devitrification, as well as liquid clusters during melting. This approach provides a detailed microscopic view of the transformation dynamics and reveals the structural signatures underlying the enhanced stability of ultrastable glasses.

II. METHODS

A. System Model

Molecules are modeled with the monatomic water model mW [39], which is described by the Stillinger-Weber [32] potential for a specific choice of the parameters. This potential includes two-body (ϕ_2) and three-body (ϕ_3) terms in the following form:

$$E = \sum_i \sum_{j>i} \phi_2(r_{ij}) + \sum_i \sum_{j \neq i} \sum_{k>j} \phi_3(r_{ij}, r_{ik}, \theta_{ijk}) \quad (1)$$

where r_{ij} is the distance between particle i and j , and θ_{ijk} is the angle formed by the triplet of particles ijk . The strength of ϕ_3 , which favors the formation of the tetrahedral angle $\theta_0 = 109.47^\circ$, is controlled by the tetrahedral parameter λ . σ is the size of particles and the cutoff is $a = 1.8\sigma$. For the following choice of the parameters (appearing in ϕ_2 and ϕ_3), $\lambda = 23.15$, $\epsilon = 6.189$ kcal/mol and $\sigma = 2.3925$ Å, the SW model reduces to the mW [39].

B. MD simulations

Molecular dynamics (MD) simulations are performed with LAMMPS [47]. The system setup is the same as that described in Ref. [31]. It consists of a simulation box with dimensions $L_x = L_y = 15\sigma = 35.89$ Å, and L_z big enough to accommodate all the particles deposited.

Periodic boundary conditions are taken along x and y . The time step is set to $dt = 5$ fs, as done in other deposition simulations of mW particles [31, 48]. The properties of the systems are computed in the core defined by all the particles forming the QG or the DG excluding those in a 3σ -thick layer in contact with the free surface and with the substrate.

The glass is deposited by sequentially injecting individual particles from random positions at the top of the box onto the substrate maintained at a constant temperature T (NVT ensemble), as detailed below. Each particle is introduced with a fixed velocity component in the deposition direction, $v_z = 0.01$ Å/fs, and random velocity components in the transverse directions (i.e., x and y), where v_x and v_y range between -0.001 and 0.001 Å/fs. This velocity distribution corresponds to a source temperature of approximately ~ 1000 K. $N = 5000$ particles are deposited with deposition rate $\gamma_{DG} = \Delta z / \Delta t$, where Δz is the size of the deposited layer along z and Δt the elapsed time.

The substrate composed of 500 particles is prepared by depositing them onto a system that already contains 500 randomly arranged particles of the same type. This initial random configuration has a density $\rho = \rho(T_m)$, where T_m is the melting temperature. To avoid mixing between the deposited particles and those in the random configuration—particularly at temperatures above T_g —each particle in the random distribution is independently tethered to its original position using a spring force with stiffness $k_{rand} = 1$. The 500 particles intended to form the substrate are deposited onto this random layer at a rate of $\gamma_{sub} = 5$ Å/ns, using the same velocity vector as employed in the primary deposition simulation. After deposition, this results in a substrate of 500 particles, to which a spring force of stiffness $k_{sub} = 1$ is independently applied to each particle, following the same procedure used for the random distribution.

The conventional quenched glass (QG), which we compare to the vapor-deposited glass (DG) in the following section, is prepared using a protocol similar to the one described in Refs. [25, 31]. The process involves taking a DG, melting it at a temperature $T_i > T_m$, and then equilibrating the system down to T_f at a cooling rate $\gamma_{QG} = \Delta T / \Delta t = (T_i - T_f) / \Delta t$. Here, Δt denotes the time required to quench the system from T_i to T_f , and for the chosen rate $\gamma_{QG} = 10$ K/ns, this corresponds to integrating $5 \cdot 10^6$ time steps. The selected quench rate, $\gamma_{QG} = 10$ K/ns, is sufficiently rapid to prevent crystallization in the mW model. It is important to note that while in the case of DG the temperature T refers to that of the substrate (which is in contact with the thermal bath), for the QG, the temperature corresponds to that of the entire system.

C. Hydrogen bond network (HBN) algorithm

To build the hydrogen bond network associated with the mW monatomic water model, we use the algorithm described by the following steps:

1. find the 4 nearest neighbors of each particle i as the neighbors with the lowest bond energy;
2. compute the tetrahedral order parameter q_i for each particle as:

$$q_i = 1 - \frac{3}{8} \sum_{j=1}^3 \sum_{k=j+1}^4 \left(\cos \theta_{ijk} + \frac{1}{3} \right)^2 \quad (2)$$

where j and k are indices going from 1 to 4, indicating the 4 nearest neighbors of particle i . θ_{ijk} is the angle formed between vectors r_{ij} and r_{ik} . $\langle q_i \rangle = 0$ for a random distribution of the 4 nearest neighbors of i , and $\langle q_i \rangle = 1$ for a perfectly tetrahedral configuration.

3. Look for non-reciprocal bonds (they should be associated with either acceptors or donors): if $q_i > q_j$ then add a bond between oxygen j and oxygen i , while if $q_j > q_i$ then remove the bond between oxygen i and oxygen j .

D. Melting

To identify liquid particles at time t we compute how many near neighbors of each particle have changed from the initial time t_0 , indicated with $C(t, t_0)$ [14, 49]. When C reaches the value 0.5 we consider a particle to be in the liquid phase. We verified that the results obtained in this work are robust against a variation in the threshold of C .

To characterize structural properties of liquid clusters during melting, we compute the radius of gyration of each cluster as $R_g = \sqrt{Tr(S)}$, where S is the gyration tensor and Tr is the trace of the associated matrix which can be written as

$$S_{\alpha\beta} = \frac{1}{2n_c^2} \sum_{i=1}^{n_c} \sum_{j=1}^{n_c} (r_{\alpha}^i - r_{\alpha}^j)(r_{\beta}^i - r_{\beta}^j) \quad (3)$$

where $\alpha, \beta = x, y, z$, and r_{α}^i is the α component of the position vector of particle i .

III. RESULTS

A. Ring statistics and thermodynamic stability

We begin by analyzing the structural characteristics of the HBN in both QG and DG by computing the fraction of bond rings of various degrees. Here, the degree refers

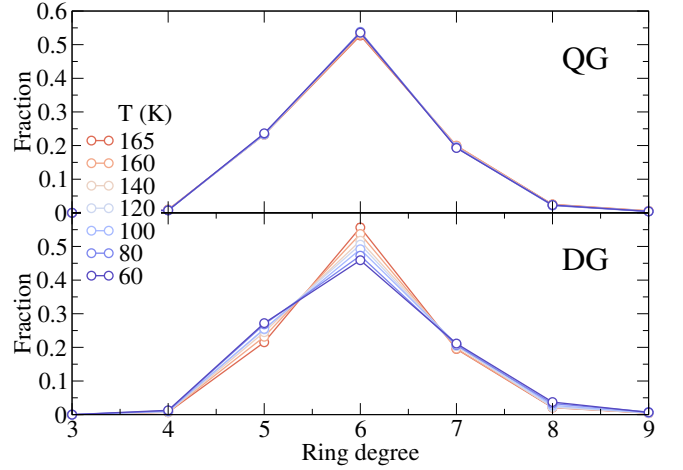


FIG. 1. Fraction of rings versus rings degree present in the core of the QG (upper panel) and the DG (lower panel) at different quench and substrate temperatures, respectively. The quench rate is $\gamma_{QG} = 10$ K/ns with a starting and final temperature of $T_i = 300$ K and $T_f = T$ (as indicated in the legend), respectively. For the DG, the deposition rate is $\gamma_{DG} = 2.5$ Å/ns.

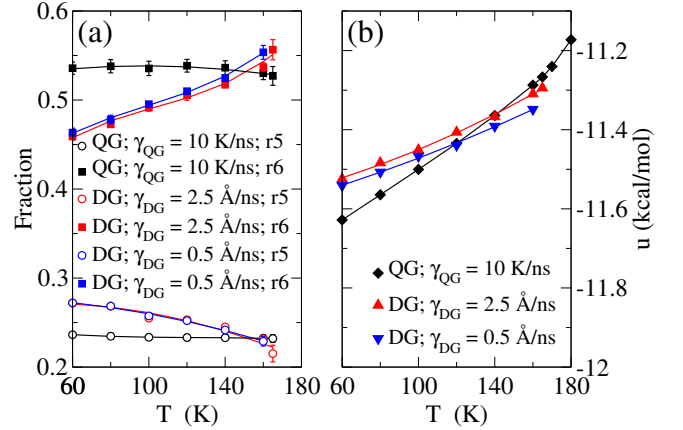


FIG. 2. Panel (a): fraction of rings of degree 5 (r5) and 6 (r6) versus temperature for the QG obtained upon quenching at $\gamma_Q = 10$ K/ns, and the DG deposited at $\gamma_D = 0.5$ and 2.5 Å/ns. Panel (b): Potential energy per particle for QG and the two DGs considered.

to the number of edges (or bonds) forming a closed loop. We first consider the QG obtained via rapid quenching at a rate of $\gamma_{QG} = 10$ K/ns and the DG formed via vapor deposition at rate $\gamma_{DG} = 2.5$ Å/ns, across a range of temperatures (see Figs. 1 and Fig. 2(a)). These results are compared with the thermodynamic stability, as captured by the potential energy per particle (Fig. 2(b)).

The temperature range examined lies below the glass transition temperature $T_g \simeq 185$ K, where the deposited glass remains in a glassy state. This range also includes the window where the DG exhibits greater sta-

bility than the QG before crystallization becomes dominant at higher temperatures. Fig. 1, upper panel, shows that the fraction of rings of different degrees in the QG are frozen at all temperatures, as expected for $T < T_g$. In contrast, from the lower panel of Fig. 1 we can see that the DG exhibits an increased fraction of rings of degree 6 and a corresponding decrease in rings of degree 5 as temperature increases, with other ring populations remaining relatively constant. In Fig. 2(a) we compare the ring statistics of the QG for $\gamma_{QG} = 10$ K/ns with the DG for $\gamma_{DG} = 0.5$ and 2.5 Å/ns. From it we can see that the fraction of 6-member rings correlates with the thermodynamic stability of the glasses as captured by the potential energy per particle versus temperature (Fig. 2(b)).

B. Devitrification under controlled heating ramps

After considering structural properties of the different glasses obtained at a specific temperature, we perform heating ramps of the QG obtained at quench rate $\gamma_{QG} = 10$ K/ns and the DG obtained at deposition rate $\gamma_{DG} = 0.5$ Å/ns using different heating rates γ_H . We are interested, on one side, in studying the devitrification process, and on the other side in the melting phenomenology in both glasses. To investigate devitrification dynamics, we perform heating ramps on QG and DG samples at two heating rates, $\gamma_H = 1$ and 10 K/ns, starting from $T_i = 160$ K (where DG is more stable than QG, but still glassy) up to $T_f = 300$ K (well above the melting point $T_m \simeq 273$ K). We consider two heating rates to observe the different devitrification pathways expected for low and high γ_H . Indeed, at low γ_H , molecules have enough time to rearrange into a crystalline structure. On the other hand, at high γ_H , the glass is brought above T_g quickly, leading to a supercooled liquid before crystallization begins. These two different behaviors are observed for several glassy materials [14, 50], including water [51, 52].

For both glasses under all conditions and heating rates, we analyze 10 independent samples. We compute the evolution with temperature of the fraction of rings of order 5, 6, 7 for all samples heated at rate $\gamma_H = 1$ K/ns for the QG (not shown) and the DG (Fig. 3), and rate $\gamma_H = 10$ K/ns for the QG (not shown) and the DG (Fig. 4).

For $\gamma_H = 1$ K/ns, both QG and DG devitrify from the glassy phase, starting to form crystallites at about the onset temperature T_o [31], with $T_o(\gamma_H = 1\text{K/ns}) \simeq 192$ K (indicated with a bold vertical orange bar in the figures). In contrast, at rate $\gamma_H = 10$ K/ns, devitrification occurs only above $T_o(\gamma_H = 10\text{K/ns}) \simeq 202$ K (indicated with a bold vertical orange bar in the figures). A relevant difference between the devitrification process undergone at the two different heating rates lies in the emergence of an intermediate supercooled liquid phase between the glassy and the crystalline phase observed only

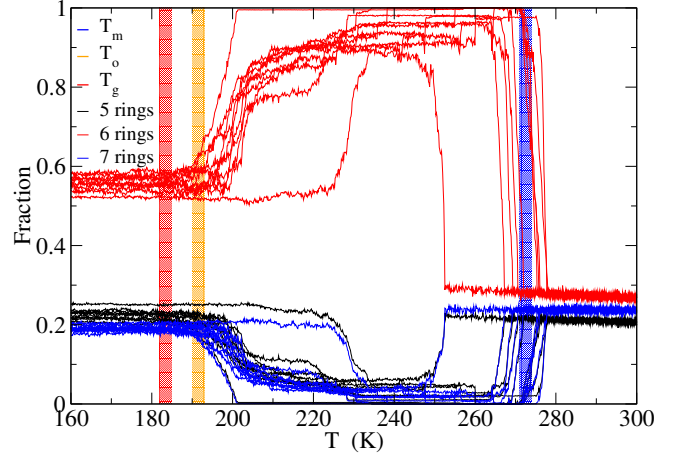


FIG. 3. Fraction of rings of degree 5, 6, and 7 versus temperature for 10 different samples of DG deposited at $\gamma_{DG} = 0.5$ Å/ns and heated from $T_i = 160$ K to $T_f = 300$ K with rate $\gamma_H = 1$ K/ns. The vertical stripes indicate the onset temperatures.

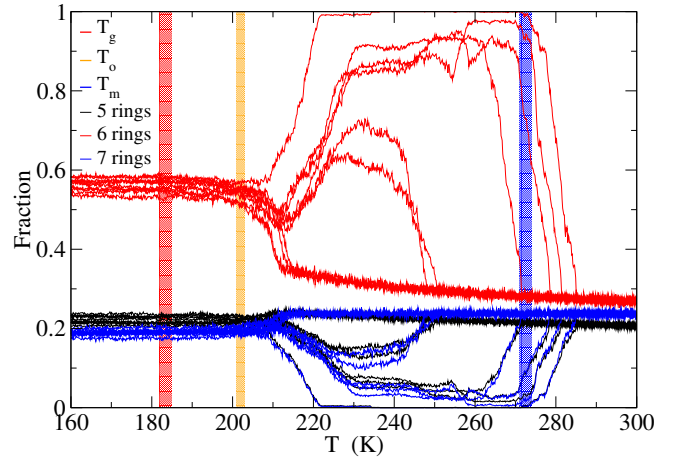


FIG. 4. Fraction of rings of degree 5, 6, and 7 versus temperature for 10 different samples of DG deposited at $\gamma_{DG} = 0.5$ Å/ns and heated from $T_i = 160$ K to $T_f = 300$ K with rate $\gamma_H = 10$ K/ns. The vertical stripes indicate the onset temperatures.

for $\gamma_H = 10$ K/ns. This intermediate phase is characterized by a drop in the fraction of 6-member rings when the temperature exceeds $T_o(\gamma_H = 10\text{K/ns})$, followed by a sharp increase, indicating crystallization, except for 3 out of 10 samples which melt without forming crystals. The mean square displacement (MSD) further supports this picture. Indeed, for the glass heated at the low rate $\gamma_H = 1$ K/ns, the MSD does not show a significant change in slope before crystallization (starting when the MSD flattens, indicating arrested dynamics, see Fig. 5 for the DG). On the other hand, for the glass heated at rate $\gamma_H = 10$ K/ns, the presence of the supercooled phase

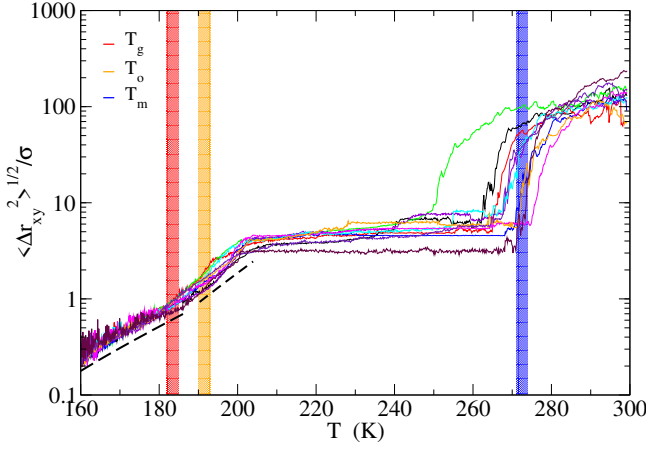


FIG. 5. Mean square displacement of 10 different samples of DG deposited at $\gamma_{DG} = 0.5 \text{ \AA/ns}$ and heated from $T_i = 160 \text{ K}$ to $T_f = 300 \text{ K}$ with rate $\gamma_H = 1 \text{ K/ns}$. The black dashed lines show the slope of the MSD vs T in the glassy phase. Dashed lines are a guide for the eyes. The vertical stripes indicate the onset temperatures.

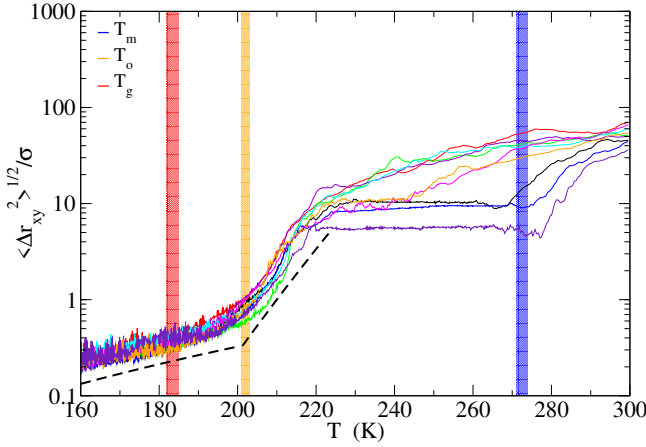


FIG. 6. Mean square displacement of 10 different samples of DG deposited at $\gamma_{DG} = 0.5 \text{ \AA/ns}$ and heated from $T_i = 160 \text{ K}$ to $T_f = 300 \text{ K}$ with rate $\gamma_H = 10 \text{ K/ns}$. The black dashed lines show the slope of the MSD vs T . The black dashed lines show the slope of the MSD vs T in the glassy and supercooled phases. Dashed lines are a guide for the eyes. The vertical stripes indicate the onset temperatures.

corresponding to the drop in the fraction of 6-member rings above T_o is confirmed by the change in slope appearing at about T_o , and signaling enhanced mobility in the supercooled liquid (see Fig. 6 for the DG).

Density profiles versus temperature also highlight this difference: the DG heated at $\gamma_H = 10 \text{ K/ns}$ (see black curve in Fig. 7(b)) that eventually crystallize show a density peak near $T = 215 \text{ K}$ before dropping as crystallization proceeds. This feature is absent at the slower heating rate $\gamma_H = 1 \text{ K/ns}$ (see Fig. 7(a)).

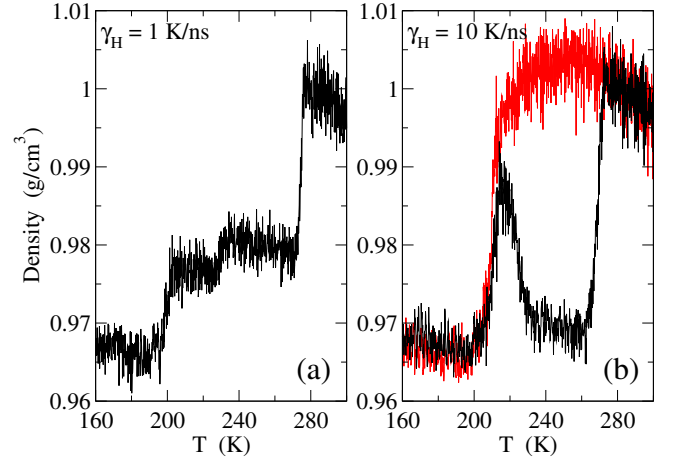


FIG. 7. Density versus temperature of typical samples of DG deposited at $\gamma_{DG} = 0.5 \text{ \AA/ns}$ and heated at rate $\gamma_H = 1 \text{ K/ns}$ (a) and $\gamma_H = 10 \text{ K/ns}$ (b). At low heating rate (a), all samples crystallize and only one of them is shown. At high heating rate (b), we show a typical crystallizing (in black) and melting without forming crystallites (in red) samples.

Note that in water the liquid phase is denser than the solid phase. In Fig. 7, liquid water at zero pressure reaches the typical density $\rho \simeq 1.0 \text{ g/cm}^3$, while the glassy phase at low temperatures assumes the typical low-density amorphous (LDA) phase density $\rho \simeq 0.96 - 0.97 \text{ g/cm}^3$.

C. Melting dynamics and kinetic stability

To probe melting behavior, we heat both QG and DG samples from $T_i = 160 \text{ K}$ to $T_f = 300 \text{ K}$ at the finite rates $\gamma_H = 1, 10 \text{ K/ns}$, and instantaneously (i.e., at infinite rate, $\gamma_H \rightarrow \infty$). A particle is identified as liquid if at least half of its neighbors differ from those at the beginning of the heating ramp (see Methods). The fraction of fluid particles N_{fluid}/N_{core} (with N_{core} the number of particles in the core, defined in Methods, and N_{fluid} the particles of the core considered fluid) during heating ramps at finite (not shown) and infinite (Fig. 8) rate shows the higher kinetic stability of the DG with respect to the QG.

At infinite heating rate, since the heating is instantaneous and then the melting rate is constant to a good approximation, the melting curves can be fitted with the Avrami law [14]: $N_{fluid}/N_{core} = 1 - \exp(-Kt^\alpha)$, with the time exponent predicted to be $\alpha = d + 1 = 4$ in three dimensions (3d). From this fit, we obtain the exponents $\alpha_{QG} \simeq 4.0$ and $\alpha_{DG} \simeq 4.4$. From arguments involving the different growing mechanisms of liquid clusters in conventional and ultrastable glasses under instantaneous heating ramps, it is expected [14] that, while the conventional glass, like the QG, should follow the Avrami law with exponent $1 + d = 4$ in 3d, the ultrastable one should

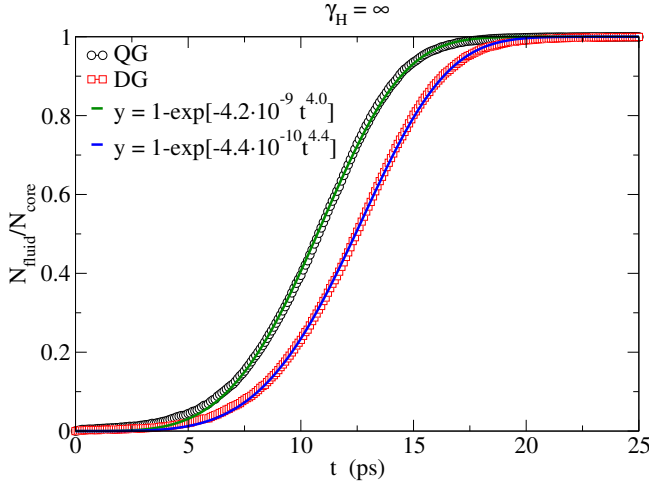


FIG. 8. Average fraction of fluid particles versus temperature for the QG and DG at infinite heating rate. The Avrami equation accurately fits the QG and DG data with an Avrami exponent of 4.0 and 4.4, respectively.

follow it with a larger value of the exponent. The value of $\alpha_{DG} \simeq 4.4$ we find in the current system is indicative of a distinct melting mechanism and a hallmark of ultrastability in the DG.

D. Glass melting and liquid clusters growth

Differences in the melting dynamics between QG and DG can be observed from snapshots of configurations taken at different temperatures for $\gamma_H = 10$ K/ns with particles colored according to the value of $0 \leq C \leq 1$ (see Methods). From snapshots (see Figs. 9, 10) we can see that, while for the QG melting initiates uniformly throughout the sample, for the DG melting preferentially begins at the free surface, consistent with the heterogeneous transformation of stable glasses into liquids beginning at the surface of the sample observed for different materials heated at high rate [2, 53, 54].

We further characterize the spatial extent of liquid regions by computing the radius of gyration R_g of liquid clusters (see Methods). In Fig. 11, we show the size n versus the normalized radius of gyration R_g/σ for the QG and DG at all heating rates considered in this work, i.e., for $\gamma_H = 1, 10, \infty$ K/ns. In all cases, clusters follow the sub-3d growth law: $n \sim R_g^{2.2}$, indicating a common geometric growth regime. The enhanced Avrami exponent observed for DG, therefore, originates from its higher kinetic stability rather than a fundamentally different cluster growth geometry.

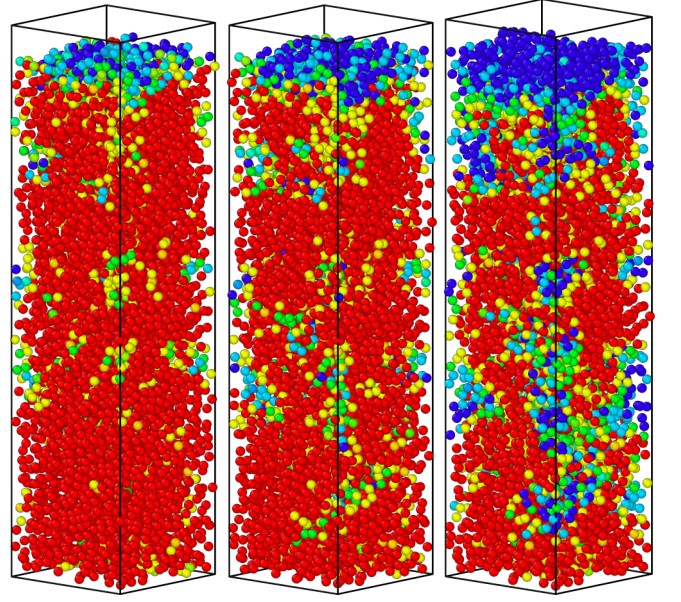


FIG. 9. Melting of the DG deposited at rate $\gamma_{DG} = 0.5$ Å/ns and heated from $T_i = 160$ K to $T_f = 300$ K at rate $\gamma_H = 10$ K/ns. From left to right, snapshots are taken at temperature $T = 180, 190, 200$ K. Colors correspond to the value of C (see Methods) going from 0 (red) to 1 (blue). Snapshots are made with Ovito [55].

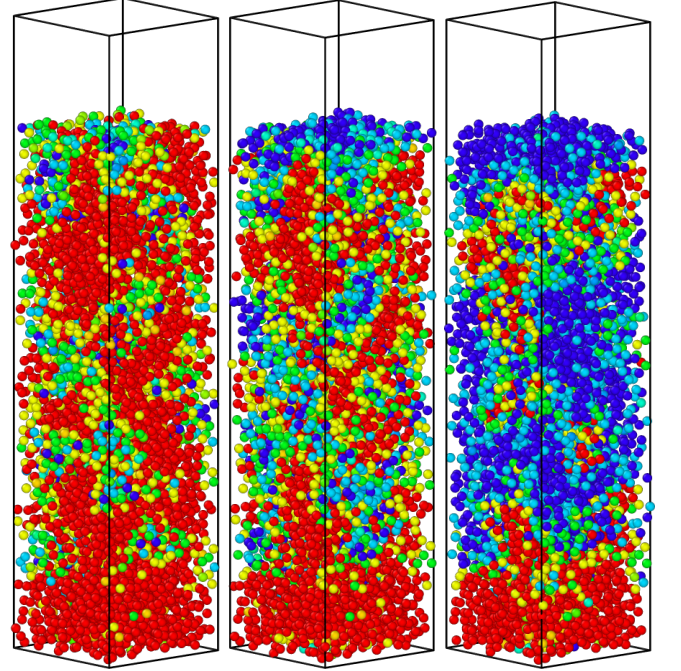


FIG. 10. Melting of the QG quenched at rate $\gamma_{QG} = 10$ K/ns and heated from $T_i = 160$ K to $T_f = 300$ K at rate $\gamma_H = 10$ K/ns. From left to right, snapshots are taken at temperature $T = 180, 190, 200$ K. Colors correspond to the value of C (see Methods) going from 0 (red) to 1 (blue).

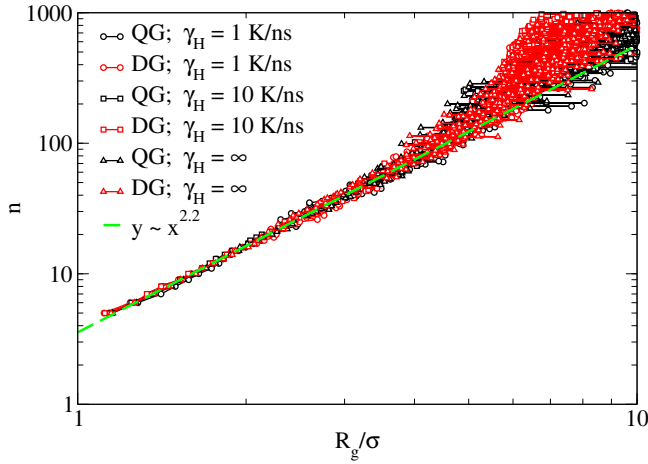


FIG. 11. Average size of fluid clusters n versus their scaled Radius of gyration R_g/σ for the QG and DG at different heating rates. The growth of the fluid clusters follows a sub-3D evolution with $n \sim R_g^{2.2}$.

E. Crystallization

Due to its tendency to spontaneously form crystalline structures within accessible simulation timescales, the mW water model has been effectively used to describe fundamental aspects of ice nucleation and growth [36–38], especially at high supercooling conditions [56, 57]. During heating ramps conducted at finite rates, most of the ten simulated samples of both the QG and DG exhibit crystallization via similar pathways and dynamics, with a few noteworthy differences. Specifically:

i) Multiple grains of randomly stacked cubic (Ic) and hexagonal (Ih) ice compete during the crystallization process (we emphasize here that geometric arguments favor polymorphism selection in molecular models of water towards Ih [58], as observed experimentally); *ii)* The non-equilibrium melting temperature of crystalline clusters—ranging from 245 K to 277 K—depends strongly on cluster size and the presence of defects; *iii)* Crystal melting generally initiates in regions with a high defect concentration, though in the absence of such regions, it typically proceeds symmetrically from the upper and lower surfaces (along the z -direction) of the cluster. Differences between the QG and DG primarily relate to the spatial location of the nucleating clusters. While nucleation in QG samples can occur throughout the bulk of the layer, approximately one-third of DG samples show a preference for nucleation near the free surface.

The role of a free surface in influencing the ice nucleation pathway remains an open question [59–61]. It is still under debate whether nucleation preferentially occurs near the free surface [62] or within the bulk [63], and whether such behavior is dependent on the model used in MD simulations [62–65]. A recent work [62] has highlighted the critical importance of 5-membered rings

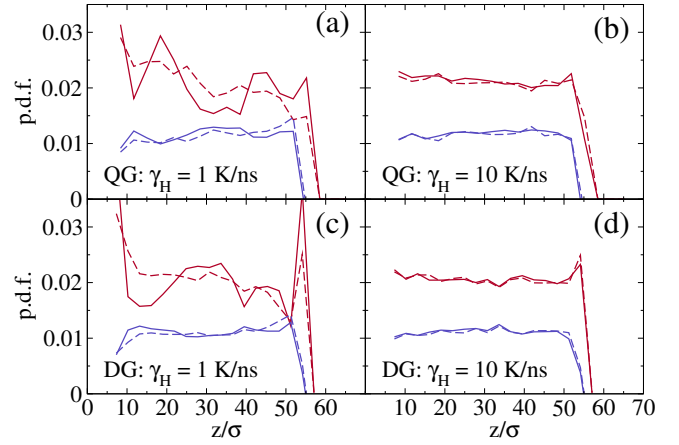


FIG. 12. Probability distribution function along the z direction of 5- (red) and 6-membered (blue) rings for the QG heated at rate (a) $\gamma_H = 1$ and (b) 10 K/ns. Similarly for the DG heated at rate (c) $\gamma_H = 1$ and (d) 10 K/ns. For a better readability, 6-membered rings curves are shifted along y of -0.01. Dashed and continuous lines refer to averages over a range of temperature of 196–202 K and 202–208 K, respectively.

(associated with precursor structures, such as ice 0-like environments [38, 66, 67]) in the crystallization process. Ref. [62] reports an excess of 5-membered rings near the free surface in MD simulations using the TIP4P/Ice water model [68], which is shown to produce nucleation pathways similar to those observed in the mW model.

Thanks to the algorithm we adopted to build the HBN from the mW point molecules configuration (see Methods), we can also study the evolution of the probability distribution function (p.d.f.) of rings of various orders across the deposition direction in both QG and DG samples for temperatures before crystallization takes place. As shown in Fig. 12, while it is difficult to establish the presence of an excess of ice-0-like structures (rich in 5-membered rings) near the free surface of the QG (a, b), our data clearly indicate this enhancement of 5-membered rings near the free surface in DG samples (c, d).

Given the limited size of our dataset (10 independent configurations), we cannot give a conclusive answer to the general problem of the ice nucleation pathway followed in the presence of a free surface. However, in agreement with Ref. [62], we definitively observe an increase in 5-membered ring precursors, along with a nucleation preference, in DG samples near the free surface. Although not the central focus of this study, these findings highlight the relevant role of stability in the pathway to nucleation in presence of a free surface worth of further investigation.

IV. CONCLUSIONS

In this work, we employed molecular dynamics simulations to investigate the differences in equilibration dynamics between conventional (quenched) and ultrastable (deposited) glasses subjected to thermal protocols. We considered a coarse-grained monatomic water model including three-body interactions, representative of a broad class of tetrahedral materials. We introduced a novel algorithm to build the hydrogen bond network from coarse-grained point-molecule configurations. This approach enabled us to analyze both the structural properties of the HBN, such as ring statistics, and the evolution of melting clusters during heating. Our key findings are as follows:

i) The population of 6-membered rings reflects the relative stability of the glasses; *ii)* Melting (transition from glassy to liquid state) and devitrification (transition from glassy to crystalline state) are observed at low and high heating rates, respectively, with the latter mediated by a transient supercooled liquid phase; *iii)* Under instantaneous heating (effectively infinite rate), the melting kinetics of the QG follows the Avrami equation, while the DG exhibits a higher Avrami exponent, indicating enhanced kinetic stability; *iv)* Melting in QG initiates in the bulk, whereas in DG it preferentially starts near the free surface, particularly under faster heating conditions; *v)* Across all samples and heating rates, liquid clusters grow via sub-three-dimensional scaling, following the relation $n \sim R_g^{2.2}$, where n is the cluster size and R_g its radius of gyration; *vi)* DG samples exhibit an excess of

5-membered rings near the free surface, consistent with their tendency to nucleate the crystal phase in this region—highlighting a distinct pathway compared to QG.

Overall, our results underscore the critical role of glass preparation protocol and interfacial effects in determining the thermal response and nucleation behavior of glassy water. The insights gained here may be relevant for understanding ultrastable glasses more broadly and for the design of materials with tailored thermal stability.

DATA AVAILABILITY

The data that support the findings of this study are available from the corresponding author upon reasonable request.

ACKNOWLEDGMENTS

We are happy to join the celebrations for the 60th birthday of Carlos Vega. We thank Andreas Neophytou for helpful discussions. F.L. and J.R. acknowledge support by ICSC – Centro Nazionale di Ricerca in High Performance Computing, Big Data and Quantum Computing, funded by European Union – NextGenerationEU, and the CINECA award under the ISCRA initiative, for the availability of high-performance computing resources and support.

-
- [1] S. F. Swallen, K. L. Kearns, M. K. Mapes, Y. S. Kim, R. J. McMahon, M. D. Ediger, T. Wu, L. Yu, and S. Satija, Organic glasses with exceptional thermodynamic and kinetic stability, *Science* **315**, 353 (2007).
 - [2] M. D. Ediger, Perspective: Highly stable vapor-deposited glasses, *J. Chem. Phys.* **147**, 210901 (2017).
 - [3] C. Rodríguez-Tinoco, M. Gonzalez-Silveira, M. A. Ramos, and J. Rodríguez-Viejo, Ultrastable glasses: new perspectives for an old problem, *Riv. del Nuovo Cim.* **45**, 325–406 (2022).
 - [4] P. Luo, S. E. Wolf, S. Govind, R. B. Stephens, D. H. Kim, C. Y. Chen, T. Nguyen, P. Wasik, M. Zhernenkov, B. McClimon, *et al.*, High-density stable glasses formed on soft substrates, *Nat. Mater.* **23**, 688 (2024).
 - [5] S. S. Dalal, A. Sepúlveda, G. K. Pribil, Z. Fakhraai, and M. D. Ediger, Density and birefringence of a highly stable α , α , β -trisinaphthylbenzene glass, *J. Chem. Phys.* **136**, 204501 (2012).
 - [6] Y. Chua, M. Ahrenberg, M. Tylinski, M. Ediger, and C. Schick, How much time is needed to form a kinetically stable glass? ac calorimetric study of vapor-deposited glasses of ethylcyclohexane, *J. Chem. Phys.* **142** (2015).
 - [7] C. Rodríguez-Tinoco, M. Gonzalez-Silveira, J. Ràfols-Ribé, G. Garcia, and J. Rodríguez-Viejo, Highly stable glasses of celecoxib: Influence on thermo-kinetic properties, microstructure and response towards crystal growth, *J. Non-Cryst. Solids* **407**, 256 (2015).
 - [8] K. R. Whitaker, M. Tylinski, M. Ahrenberg, C. Schick, and M. D. Ediger, Kinetic stability and heat capacity of vapor-deposited glasses of o-terphenyl, *J. Chem. Phys.* **143**, 084511 (2015).
 - [9] M. Tylinski, Y. Z. Chua, M. S. Beasley, C. Schick, and M. D. Ediger, Vapor-deposited alcohol glasses reveal a wide range of kinetic stability, *The Journal of Chemical Physics* **145**, 174506 (2016).
 - [10] C. J. Fullerton and L. Berthier, Density controls the kinetic stability of ultrastable glasses, *Europhys. Lett.* **119** (2017).
 - [11] A. Vila-Costa, M. Gonzalez-Silveira, C. Rodríguez-Tinoco, M. Rodríguez-López, and J. Rodríguez-Viejo, Emergence of equilibrated liquid regions within the glass, *Nature Physics* **19**, 114 (2023).
 - [12] M. Ruiz-Ruiz, A. Vila-Costa, T. Bar, C. Rodríguez-Tinoco, M. Gonzalez-Silveira, J. A. Plaza, J. Alcalá, J. Fraxedas, and J. Rodríguez-Viejo, Real-time microscopy of the relaxation of a glass, *Nat. Phys.* **19**, 1509 (2023).
 - [13] E. Flenner, L. Berthier, P. Charbonneau, and C. J. Fullerton, Front-mediated melting of isotropic ultrastable glasses, *Phys. Rev. Lett.* **123**, 175501 (2019).
 - [14] C. Herrero, C. Scalliet, M. D. Ediger, and L. Berthier, Two-step devitrification of ultrastable glasses, *Proc.*

- Natl. Acad. Sci. U.S.A. **120**, e2220824120 (2023).
- [15] R. N. Chacko, F. m. c. P. Landes, G. Biroli, O. Dauchot, A. J. Liu, and D. R. Reichman, Dynamical facilitation governs the equilibration dynamics of glasses, *Phys. Rev. X* **14**, 031012 (2024).
 - [16] K. L. Kearns, M. Ediger, H. Huth, and C. Schick, One micrometer length scale controls kinetic stability of low-energy glasses, *J. Phys. Chem. Lett.* **1**, 388 (2010).
 - [17] A. Sepúlveda, S. F. Swallen, and M. D. Ediger, Manipulating the properties of stable organic glasses using kinetic facilitation, *J. Chem. Phys.* **138** (2013).
 - [18] M. Fanfoni and M. Tomellini, The johnson-mehl-avrami-kohnogorov model: a brief review, *Il Nuovo Cimento D* **20**, 1171 (1998).
 - [19] J. D. Stevenson and P. G. Wolynes, On the surface of glasses, *J. Chem. Phys.* **129** (2008).
 - [20] I. Lyubimov, M. D. Ediger, and J. J. de Pablo, Model vapor-deposited glasses: Growth front and composition effects, *J. Chem. Phys.* **139** (2013).
 - [21] D. R. Reid, I. Lyubimov, M. Ediger, and J. J. De Pablo, Age and structure of a model vapour-deposited glass, *Nat. Commun.* **7**, 13062 (2016).
 - [22] L. Berthier, P. Charbonneau, E. Flenner, and F. Zamponi, Origin of ultrastability in vapor-deposited glasses, *Phys. Rev. Lett.* **119**, 188002 (2017).
 - [23] S. Samanta, G. Huang, G. Gao, Y. Zhang, A. Zhang, S. Wolf, C. N. Woods, Y. Jin, P. J. Walsh, and Z. Fakhraai, Exploring the importance of surface diffusion in stability of vapor-deposited organic glasses, *J. Phys. Chem. B* **123**, 4108 (2019).
 - [24] T. J. Ferron, J. L. Thelen, K. Bagchi, C. Deng, E. Gann, J. J. de Pablo, M. Ediger, D. F. Sunday, and D. M. DeLongchamp, Characterization of the interfacial orientation and molecular conformation in a glass-forming organic semiconductor, *ACS Appl. Mater. Interfaces* **14**, 3455 (2022).
 - [25] F. Leoni, F. Martelli, C. P. Royall, and J. Russo, *Phys. Rev. Lett.* **130**, 198201 (2023).
 - [26] S. Léonard and P. Harrowell, Macroscopic facilitation of glassy relaxation kinetics: Ultrastable glass films with frontlike thermal response, *J. Chem. Phys.* **133** (2010).
 - [27] A. S. Keys, L. O. Hedges, J. P. Garrahan, S. C. Glotzer, and D. Chandler, Excitations are localized and relaxation is hierarchical in glass-forming liquids, *Phys. Rev. X* **1**, 021013 (2011).
 - [28] C. Herrero and L. Berthier, Direct numerical analysis of dynamic facilitation in glass-forming liquids, *Phys. Rev. Lett.* **132**, 258201 (2024).
 - [29] R. Candelier, A. Widmer-Cooper, J. K. Kummerfeld, O. Dauchot, G. Biroli, P. Harrowell, and D. R. Reichman, Spatiotemporal hierarchy of relaxation events, dynamical heterogeneities, and structural reorganization in a supercooled liquid, *Phys. Rev. Lett.* **105**, 135702 (2010).
 - [30] F. Leoni, J. Russo, F. Sciortino, and T. Yanagishima, Generating ultrastable glasses by homogenizing the local virial stress, *Phys. Rev. Lett.* **134**, 128201 (2025).
 - [31] F. Leoni, F. Martelli, and J. Russo, Correlating ultrastability with fragility and surface mobility in vapor deposited tetrahedral glasses, *J. Phys. Chem. Lett.* **15**, 8444 (2024).
 - [32] F. H. Stillinger and T. A. Weber, Computer simulation of local order in condensed phases of silicon, *Phys. Rev. B* **31**, 5262 (1985).
 - [33] V. Molinero, S. Sastry, and C. A. Angell, Tuning of tetrahedrality in a silicon potential yields a series of monatomic (metal-like) glass formers of very high fragility, *Phys. Rev. Lett.* **97**, 075701 (2006).
 - [34] F. Smallenburg, L. Filion, and F. Sciortino, Erasing no-man's land by thermodynamically stabilizing the liquid-liquid transition in tetrahedral particles, *Nature physics* **10**, 653 (2014).
 - [35] J. Russo, K. Akahane, and H. Tanaka, Water-like anomalies as a function of tetrahedrality, *Proc. Natl. Acad. Sci. U.S.A.* **115**, E3333 (2018).
 - [36] E. B. Moore and V. Molinero, Structural transformation in supercooled water controls the crystallization rate of ice, *Nature* **479**, 506 (2011).
 - [37] L. Lupi, A. Hudait, B. Peters, M. Grünwald, R. Gotchy Mullen, A. H. Nguyen, and V. Molinero, Role of stacking disorder in ice nucleation, *Nature* **551**, 218 (2017).
 - [38] F. Leoni and J. Russo, Nonclassical nucleation pathways in stacking-disordered crystals, *Phys. Rev. X* **11**, 031006 (2021).
 - [39] V. Molinero and E. B. Moore, Water modeled as an intermediate element between carbon and silicon, *J. Phys. Chem. B* **113**, 4008 (2009).
 - [40] C. M. Tonauer, L.-R. Fidler, J. Giebelmann, K. Yamashita, and T. Loerting, Nucleation and growth of crystalline ices from amorphous ices, *J. Chem. Phys.* **158**, 141001 (2023).
 - [41] C. Alba-Simionesco, P. Judeinstein, S. Longeville, O. Osta, F. Porcher, F. Caupin, and G. Tarjus, Interplay of vitrification and ice formation in a cryoprotectant aqueous solution at low temperature, *Proc. Natl. Acad. Sci. U.S.A.* **119**, e2112248119 (2022).
 - [42] F. Martelli, F. Leoni, F. Sciortino, and J. Russo, Connection between liquid and non-crystalline solid phases in water, *J. Chem. Phys.* **153** (2020).
 - [43] F. Martelli, Unravelling the contribution of local structures to the anomalies of water: The synergistic action of several factors, *The Journal of chemical physics* **150** (2019).
 - [44] J. Russo, F. Leoni, F. Martelli, and F. Sciortino, The physics of empty liquids: from patchy particles to water, *Rep. Prog. Phys.* **85**, 016601 (2022).
 - [45] A. Neophytou, D. Chakrabarti, and F. Sciortino, Topological nature of the liquid-liquid phase transition in tetrahedral liquids, *Nat. Phys.* **18**, 1248 (2022).
 - [46] Y. A. Gutiérrez Fosado, D. Michieletto, and F. Martelli, Link to densify: Topological transitions and origin of hysteresis during the compression and decompression of amorphous ices, *Phys. Rev. Lett.* **133**, 266102 (2024).
 - [47] A. P. Thompson, H. M. Aktulga, R. Berger, D. S. Bolintineanu, W. M. Brown, P. S. Crozier, P. J. in 't Veld, A. Kohlmeyer, S. G. Moore, T. D. Nguyen, R. Shan, M. J. Stevens, J. Tranchida, C. Trott, and S. J. Plimpton, LAMMPS - a flexible simulation tool for particle-based materials modeling at the atomic, meso, and continuum scales, *Comp. Phys. Comm.* **271**, 108171 (2022).
 - [48] L. Lupi, N. Kastelowitz, and V. Molinero, Vapor deposition of water on graphitic surfaces: Formation of amorphous ice, bilayer ice, ice i, and liquid water, *J. Chem. Phys.* **141** (2014).
 - [49] K. S. Sarkar, K. A. Interiano-Alberto, J. F. Douglas, and R. S. Hoy, Quantitative relations between nearest-neighbor persistence and slow heterogeneous dynamics in

- supercooled liquids, *J. Chem. Phys.* **162**, 194502 (2025).
- [50] D. V. Louzguine-Luzgin and A. Inoue, A glance on the glass-transition phenomenon from the viewpoint of devitrification, *J. Alloys Compd* **434-435**, 121 (2007).
- [51] S. N. Bhat, A. Sharma, and S. V. Bhat, Vittrification and glass transition of water: Insights from spin probe esr, *Phys. Rev. Lett.* **95**, 235702 (2005).
- [52] L. Kringle, W. A. Thornley, B. D. Kay, and G. A. Kimmel, Reversible structural transformations in supercooled liquid water from 135 to 245 k, *Science* **369**, 1490 (2020).
- [53] S. F. Swallen, K. Traynor, R. J. McMahon, M. D. Ediger, and T. E. Mates, Stable glass transformation to supercooled liquid via surface-initiated growth front, *Phys. Rev. Lett.* **102**, 065503 (2009).
- [54] R. Kaur, D. Bhattacharya, U. S. Cubeta, and V. Sadtchenko, Glass softening in the limit of high heating rates: Heterogeneous devitrification kinetics on nano, meso, and micrometer scale, *J. Chem. Phys.* **158**, 164507 (2023).
- [55] A. Stukowski, Visualization and analysis of atomistic simulation data with OVITO—the open visualization tool, *Modelling and Simulation in Materials Science and Engineering* **18**, 015012 (2009).
- [56] J. R. Espinosa, C. Navarro, E. Sanz, C. Valeriani, and C. Vega, On the time required to freeze water, *J. Chem. Phys.* **145**, 211922 (2016).
- [57] I. Sanchez-Burgos, A. R. Tejedor, C. Vega, M. M. Conde, E. Sanz, J. Ramirez, and J. R. Espinosa, Homogeneous ice nucleation rates for mw and tip4p/ice models through lattice mold calculations, *J. Chem. Phys.* **157**, 094503 (2022).
- [58] F. Martelli and J. C. Palmer, Signatures of sluggish dynamics and local structural ordering during ice nucleation, *The Journal of Chemical Physics* **156** (2022).
- [59] A. Tabazadeh, Y. S. Djikaev, and H. Reiss, Surface crystallization of supercooled water in clouds, *Proc. Natl. Acad. Sci. U.S.A.* **99**, 15873 (2002).
- [60] D. Duft and T. Leisner, Laboratory evidence for volume-dominated nucleation of ice in supercooled water microdroplets, *Atmos. Chem. Phys.* **4**, 1997 (2004).
- [61] C. Gurganus, A. B. Kostinski, and R. A. Shaw, Fast imaging of freezing drops: No preference for nucleation at the contact line, *J. Phys. Chem. Lett.* **2**, 1449 (2011).
- [62] G. Sun and H. Tanaka, Surface-induced water crystallisation driven by precursors formed in negative pressure regions, *Nat. Commun.* **15**, 6083 (2024).
- [63] A. Haji-Akbari and P. G. Debenedetti, Computational investigation of surface freezing in a molecular model of water, *Proc. Natl. Acad. Sci. U.S.A.* **114**, 3316 (2017).
- [64] T. Li, D. Donadio, and G. Galli, Ice nucleation at the nanoscale probes no man’s land of water, *Nat. Commun.* **4**, 1887 (2013).
- [65] A. Haji-Akbari, R. S. DeFever, S. Sarupria, and P. G. Debenedetti, Suppression of sub-surface freezing in free-standing thin films of a coarse-grained model of water, *Phys. Chem. Chem. Phys.* **16**, 25916 (2014).
- [66] J. Russo, F. Romano, and H. Tanaka, New metastable form of ice and its role in the homogeneous crystallization of water, *Nat. Mater.* **13**, 733 (2014).
- [67] F. Leoni, R. Shi, H. Tanaka, and J. Russo, Crystalline clusters in mw water: Stability, growth, and grain boundaries, *J. Chem. Phys.* **151** (2019).
- [68] J. Abascal, E. Sanz, R. García Fernández, and C. Vega, A potential model for the study of ices and amorphous water: Tip4p/ice, *J. Chem. Phys.* **122** (2005).